PCCP

Accepted Manuscript

ROYAL SOCIETY OF CHEMISTRY

www.rsc.org/pccp

PCCP

RSCPublishing

ARTICLE

Synthesis of porous Co_3O_4 nanonetworks to detect toluene at low concentration†

Cite this: DOI: 10.1039/x0xx00000x

Changhui Zhao,[a] Baoyu Huang,[a] Jinyuan Zhou,*[a] and Erqing Xie*[a]

Received 00th January 2012,
Accepted 00th January 2012

DOI: 10.1039/x0xx00000x

www.rsc.org/

Porous Co_3O_4 nanonetworks (NNWs), converted from precursor CoOOH nanosheets, have been synthesized via a controllable chemical reaction route followed by calcination at 400 ℃ in air. The morphologies and microstructures of the precursor nanosheets and the final products were characterized by high-resolution transmission electron microscopy and X-ray diffraction, respectively. The growth mechanism of CoOOH nanosheets and the structural transformation processes of NNWs were investigated in detail. Significantly, the porous Co_3O_4 NNWs based sensor showed an enhanced response to toluene gas at low concentration, which was mainly due to their porous neck-connected networks.

Introduction

As a multifunctional p-type semiconductor, spinel Co_3O_4 has attracted much attention in the fields of catalysts, magnets, electrochromic, Li-ion batteries, supercapacitors, and gas sensors.[1-7] In particular, the gas-sensing properties of various Co_3O_4 micro- and nanostructures have been widely explored, such as nanorods, nanofibers, nanosheets, and hollow microspheres.[8-14] Among them, porous architectures are expected and confirmed to play a key role in improving the sensor performances, due to their high surface area, high gas transmission abilities, and special grain interconnectivity.[15-17] Up till now, many efforts have been endeavored to construct Co_3O_4 nanoscale building blocks into complex hierarchical nanostructures, including hydrothermal, solvothermal, electrospinning, template/template-free, chemical deposition, and the combined methods.[9, 10, 18-24] But it is still a great challenge to develop a simple, economical and large-scale synthetic method for the construction of porous Co_3O_4 nanostructures.

Previously our group found that porous NiO nanosheets with neck-connected networks could be prepared by a simplified chemical bath deposition (CBD) method, and these porous networks exhibited enhanced ethanol sensing performances.[25] In this work, ultrathin CoOOH nanosheets have been synthesized at proper chemical reaction conditions, while transformed into porous Co_3O_4 nanonetworks (NNWs) after calcination at 400 ℃ for 2 h. The obtained porous NNWs are constructed by numerous neck-connected Co_3O_4 nanoparticles, which lie between porous nanosheets and nanoparticles. To the best of authors' knowledge, this is a new strategy to achieve the porous Co_3O_4 NNWs by rebuilding the precursor nanosheets. The growth mechanism of CoOOH nanosheets and the structural transformation processes of NNWs were mainly investigated. Furthermore, the gas-sensing results indicated that the sensor based on porous NNWs exhibited high performances to toluene at a low operating temperature of 150 ℃.

Experimental details

Synthesis

All the reagents in our experiment were of analytical grade and used without any further purification. In brief, 10 mL of 0.1 M cobalt nitrate hexahydrate ($Co(NO_3)_2\cdot 6H_2O$) and 1 mL of aqueous ammonia ($NH_3\cdot H_2O$, 25~28%) were mixed, followed with a continual stirring for 5 min. Then 5 mL of 0.25 M potassium persulfate ($K_2S_2O_8$) was added into the mixture. After stirring for another 20 min, black precipitates were obtained and respectively washed with deionized water and acetone several times, and slowly dried into a type of puffed precursors. All operations were carried out at room temperature. Finally, the obtained precursors were calcined at 350, 400, and 500 ℃ for 2 h in air, respectively.

Characterizations and gas-sensing measurements

The microstructures and morphologies of products were characterized by X-ray diffraction (XRD, Rigaku, D/max-2400) and high-resolution transmission electron microscope (HRTEM, FEI, Tecnai G2 F30), respectively. The specific surface area was carried out using the Brunauer–Emmett–Teller (BET, ASAP 2020) method based on nitrogen (N_2) gas adsorption. Gas-sensing properties were measured with a WS-30A system (Weisheng Instruments Co.). As described in our previous work, the final products were mixed with proper amount of binder, and pasted to an alumina tube with a pair of Au electrodes. Then all the sensors were heat treated at 350 ℃ in air for 2 h to remove the organic content of the paste. The sensor response ($S = R_g/R_a$, where R_g and R_a are the sensor resistance in mixed gas and in air, respectively) was measured at an operating temperature varies from 100 ℃ to 175 ℃ (RH~

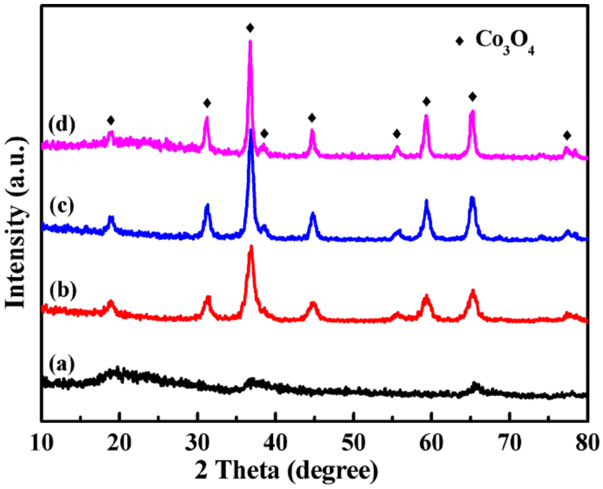

Fig. 1 XRD patterns of (a) the as-prepared precursors at room temperature, and the Co_3O_4 products calcined for 2 h at (b) 350 ℃, (c) 400 ℃, and (d) 500 ℃, respectively.

25%).

Results and discussion

Structures of the samples

The as-prepared and calcined products were characterized using X-ray diffraction (XRD), as shown in Fig. 1. The XRD pattern of the as-prepared precursors (curve a) shows a broad peak and other two low peaks. More data can be seen in Fig. S1 in ESI†, which can be indexed to CoOOH (JCPDS 07-0169). TEM image in Fig. S1a reveals that the as-prepared samples are comprised of ultrathin CoOOH nanosheets, and HRTEM image in Fig. S1b shows that the precursors are of low crystallinity, which is consistent with the XRD pattern above and due to the low reaction temperature. Moreover, the selected-area electron diffraction (SAED) pattern inset in Fig. S1b suggests that the nanosheets are polycrystalline. These results imply that ultrathin CoOOH nanosheets can be synthesized using a controllable chemical reaction process at room temperature. Once calcined at 350, 400, and 500 ℃ in air (corresponding to curves b–d, respectively), all of characteristic peaks can be assigned to the spinel structure of Co_3O_4 (JCPDS 42-1467). In addition, the peaks of Co_3O_4 become sharp with the increase of calcination temperatures from 350 to 500 ℃, mainly owing to a faster crystal growth rate at a higher temperature.[26] EDX analysis (Fig. S2, ESI†) shows the presence of Co and O without other impurities (C and Cu peaks in EDX come from the copper-carbon grid for TEM).

To reveal the formation mechanism of CoOOH nanosheets, the TEM observations of the precursors collected at different moments after adding 5 mL of 0.25 M $K_2S_2O_8$ are shown in Fig. 2. Before adding $K_2S_2O_8$, the green precursor nanosheets and some bursa bubbles are observed (Fig. 2a and b). In Fig. 2c, it is hard to find bursa bubbles in the precursors after adding $K_2S_2O_8$ 5 min later. Further observation from Fig. 2d can be seen that the surface and edge of a nanosheet is very rough, namely the self-assembly complex nanostructure is connected through a certain way as to reduce the surface free energy of the whole system.[27] When the reaction reaches a plateau at 20 min, the surfaces of CoOOH nanosheets become smooth and the edges become neat (Fig. 2e and f). Similar reactions (Reaction (1) and Reaction (2), as follows) were reported previously.[3]

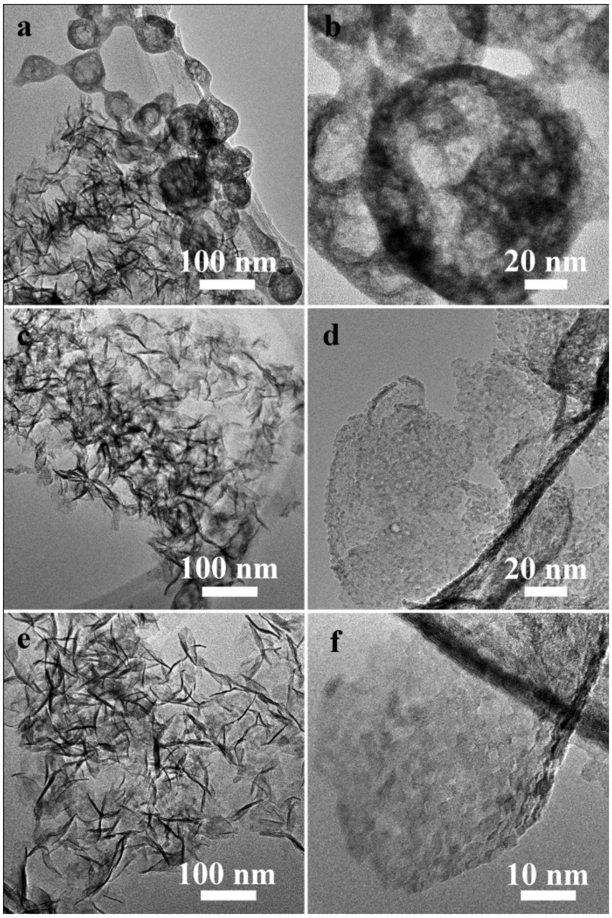

Fig. 2 TEM images of the precursors collected at different moments after adding 5 mL of $K_2S_2O_8$: (a, b) 0 min; (c, d) 5 min; (e, f) 20 min.

$$[Co(H_2O)_{6-x}(NH_3)_x]^{2+} + 2OH^- \leftrightarrow Co(OH)_2 + (6-x)H_2O + xNH_3 \tag{1}$$

$$2Co(OH)_2 + S_2O_8^{2-} \rightarrow 2CoOOH + 2SO_4^{2-} + 2H^+ \tag{2}$$

Co^{2+} can react with aqueous ammonia, and produce green $Co(OH)_2$ precursors (nanosheets and bubbles in Fig. 2a and b). The Reaction (1) is reversible, and superfluous ammonia can drive the reaction to the left, which leads to the dissolution of precursor $Co(OH)_2$ into the soluble cobalt ammonia complex ($[Co(H_2O)_{6-x}(NH_3)_x]^{2+}$). In the previous report, Kandalkar *et al.* have directly prepared CoOOH through the conversion of the $[Co(NH_3)_6]^{2+}$ at 60 ℃.[28] However, in this study, the reaction temperature was kept at room temperature. The obtained precursor $Co(OH)_2$ nanosheets are metastable and most of precursors can be simultaneously dissolved during washing with deionized water. In an attempt to overcome this shortcoming, Hosono *et al.* have applied an air-oxidation method to convert layered hydroxide cobalt acetate (LHCA) into a relatively stable CoOOH phase.[29] Given this, the addition of $K_2S_2O_8$ (a strong oxidizing agent) can also drive Reaction (2) to the right, and ensures a simple, controllable chemical reaction. As mentioned above, it is worthy of note that too much aqueous ammonia will inhibit the Reaction (1) and

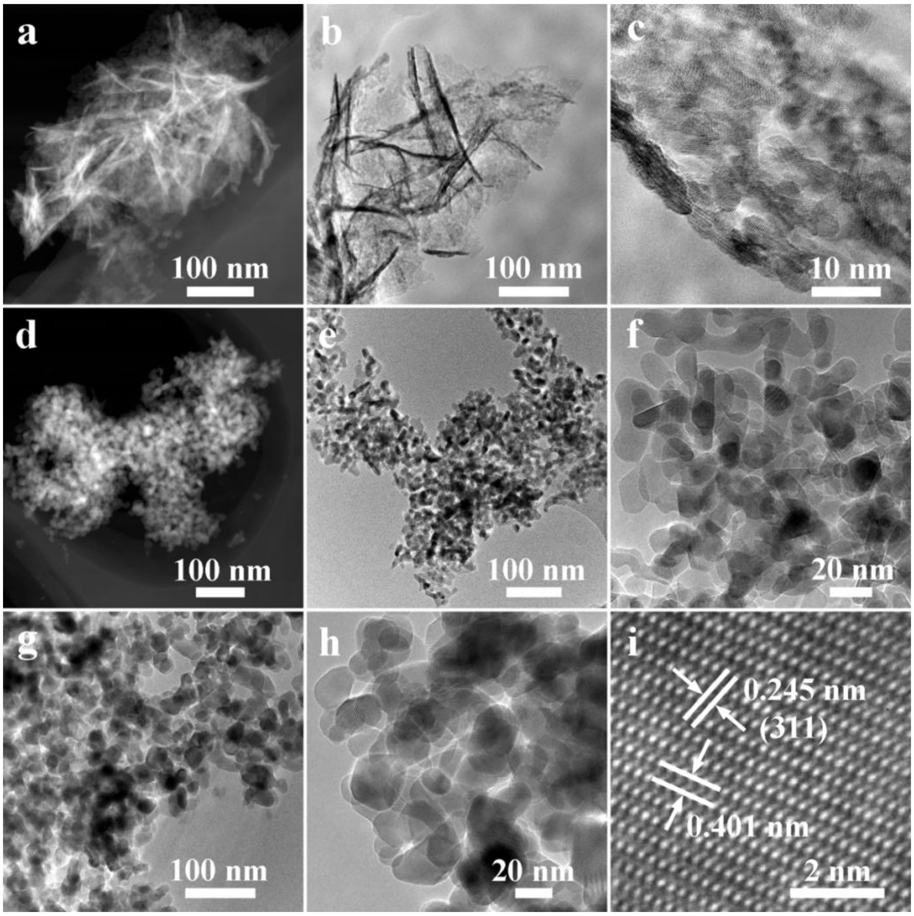

Fig. 3 STEM and TEM images of Co_3O_4 obtained at (a-c) 350 ℃, (d-f) 400 ℃, and (g and h) 500 ℃, respectively. (i) HRTEM image of a Co_3O_4 nanoparticle.

restricts indirectly the Reaction (2), even no precursor CoOOH nanosheets are formed. In turn, no any precursors formed without the addition of aqueous ammonia (just adding 5 mL of 0.25 M $K_2S_2O_8$), which means precipitation reactions are stopped completely. Thus controlling the addition amount of ammonia is very critical.

Fig. 3 shows the typical high-angle annular dark-field scanning TEM (HADDF-STEM) and TEM images of the Co_3O_4 products calcined at different temperatures. Obviously, the Co_3O_4 products maintained the lamellar structure of the precursor CoOOH nanosheets at 350 ℃ (Fig. 3a and b). It can be seen from Fig. 3c that the thickness of nanosheets increases slightly and the edges tend to become irregular. However, when the temperature reached 400 ℃, the nanosheets completely decomposed into nanoparticles (Fig. 3d–f). Different from others' reports, the nanoparticles in Fig. 3f prefer to form porous neck-connected networks, rather than form nanoparticle aggregates. Fig. S3 in ESI† shows a STEM image of Co_3O_4 products calcined at 400 ℃, which confirms the porous

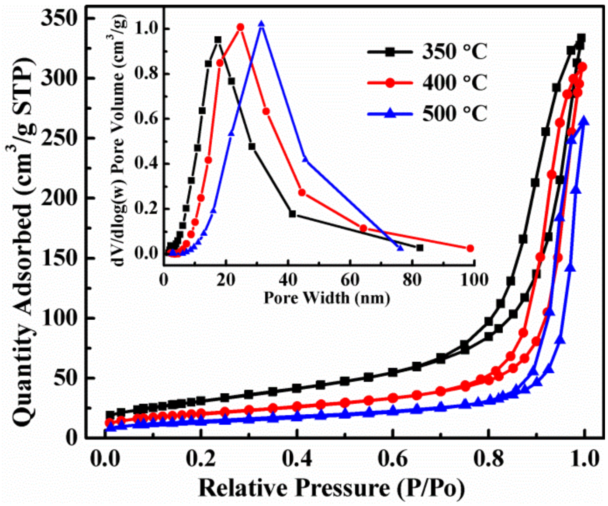

Fig. 4 N_2 adsorption–desorption isotherms and BJH pore–size–distribution curves (inset) of the samples.

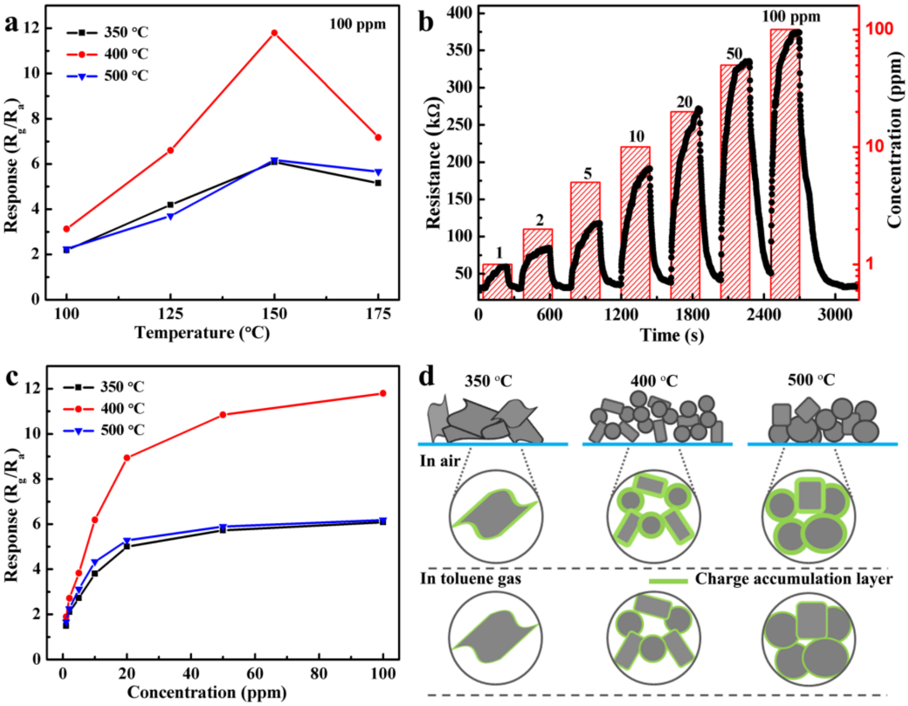

Fig. 5 (a) Response of sensors toward toluene as a function of operating temperature; (b) a typical transient curve of the sensor based on porous Co_3O_4 nanonetworks toward toluene at 150 ℃; (c) responses of sensors *versus* toluene concentration; (d) schematic illustrations of three different sensors.

structure and the puffed products. In addition, the nanoparticles become more compact at a calcination temperature of 500 ℃ (Fig. 3g and h). The increased grain size is also consistent with the results of XRD characterization in Fig. 1. The HRTEM image of a Co_3O_4 nanoparticle (Fig. 3i) shows a discerned lattice spacing of 0.245 nm, which agrees well with the (311) plane, and the lattice spacing of 0.401 nm corresponds to a double d-spacing of (400) plane.

To obtain an insight into the porous structure of the samples, the N_2 adsorption and desorption isotherms were measured at 77 K. The N_2 adsorption–desorption isotherms of the Co_3O_4 products calcined at 350, 400, and 500 ℃ are shown in Fig. 4. The BET surface area of the Co_3O_4 NNWs is ~72.89 m^2 g^{-1}, which is 43.5% higher than that of compact Co_3O_4 (~50.78 m^2 g^{-1}, 500 ℃) and is obviously lower than that of Co_3O_4 nanosheets (~114.43 m^2 g^{-1}, 350 ℃). Accordingly, the shape of the hysteresis loops is of a type H3, ascribed to the type IV isotherms, indicating the existence of mesoporous structure (2~50 nm, pore width). The inset of Fig. 4 compares the Barrett–Joyner–Halenda (BJH) pore-size distribution plots of the samples, which indicates that the material contains an average pore size of 14.31 nm for Co_3O_4 nanosheets, 21.48 nm for Co_3O_4 NNWs, and lastly, 28.44 nm for compact Co_3O_4 nanoparticles. Above all, the BET surface area decreases with the increase of calcination temperature, which are corresponding to the TEM images in Fig. 3. The pore-size-distribution results also reveal the influence of calcination temperature on the porous structure of Co_3O_4.

Gas-sensing properties

Toluene ($C_6H_5CH_3$) was chosen as a target gas because of its harmful to human beings even at very low concentrations, which has been widely used in chemical industry and found to be neurotoxic (paralysis of the central nervous system). The lowest observed adverse effect level (LOAEL) of chronic occupational toluene exposure is 332 mg m^{-3} (88 ppm).[30] Thus the efficient detection of toluene gas becomes very necessary for both environment and our own humanity.

To determine the optimum operating temperature, the response of the sensors (Co_3O_4 calcined at 350, 400, and 500 ℃, respectively, in Fig. 5a) to 100 ppm toluene was tested as a function of operating temperature (100~175 ℃). The responses increase with operating temperatures, then reach their maximum values at 150 ℃, and decrease at 175 ℃. Therefore, 150 ℃ is shosen as the optimum operating temperature and used for further characterization the gas-sensing properties of above three sensors. The corresponding response is 6.08, 11.79, and 6.18, respectively. As shown in Fig. 5b, the response and recovery behaviors of Co_3O_4 NNWs based sensor are investigated in the presence of different concentrations of

Table 1 Toluene sensing characteristics of Co_3O_4-based sensors surveyed in literatures and in this work

Materials	Gas concentration (ppm)	Temperature (℃)	Response (R_g/R_a)	S_{BET} ($m^2\ g^{-1}$)	Reference
Co_3O_4 hollow nanospheres	100	100	~5.85	120	[13]
Co_3O_4 nanocubes	100	200	~4.8	–	[31]
Co_3O_4 nanorod arrays	500	160	8.6	12.2	[32]
Ordered mesoporous Co_3O_4	100	190	23.55	102.7	[33]
Nanoparticle-assembled Co_3O_4 nanorods	100	200	26	–	[34]
Co_3O_4 NNWs	100	150	11.79	72.89	This work
Co_3O_4 nanosheets	100	150	6.08	114.43	This work

toluene (1~100 ppm) at 150 ℃. The sensor resistance increases in toluene gas (R_g) and decreases back to its initial resistance in air ($R_a \approx 30.98$ kohm) with the removal of toluene, which shows typical p-type behavior of Co_3O_4.

The relationships between concentrations and responses to toluene are shown in Fig. 5c. From the three curves, the responses increase rapidly at low toluene concentrations (< 20 ppm). Above 50 ppm, for all sensors, the responses increase slowly with increasing the toluene concentrations, indicating a gradual saturation of the sensors toward 100 ppm. The responses of the sensors versus the toluene concentrations range from 1 to 1000 ppm are shown in Fig. S4 in ESI†. Obviously, porous Co_3O_4 NNWs based sensor shows the highest response (1000 ppm, 12.58). This suggests that the sensors in our experiment are favorable to detect toluene with low concentration. The inset of Fig. S4 shows that the Co_3O_4 NNWs based sensor exhibits a good stability to 100 ppm toluene on repeat measurement in three weeks. To eliminate the affects of other gases (i.e., ammonia, hydrogen sulfide, acetone, hydrogen, and methane, seen in Fig. 6), the sensor response to 100 ppm of above five gases is 1.10, 2.30, 5.73, 1.09, and 1.16, respectively. All of the gases are detected at 150 ℃, and the sensor based on Co_3O_4 NNWs shows almost insensitive to ammonia, hydrogen, and methane, and obtains lower responses to hydrogen sulfide and acetone. Moreover, it can also be estimated that the selectivity of the sensor to toluene against other five gases is exceeding 2 times.

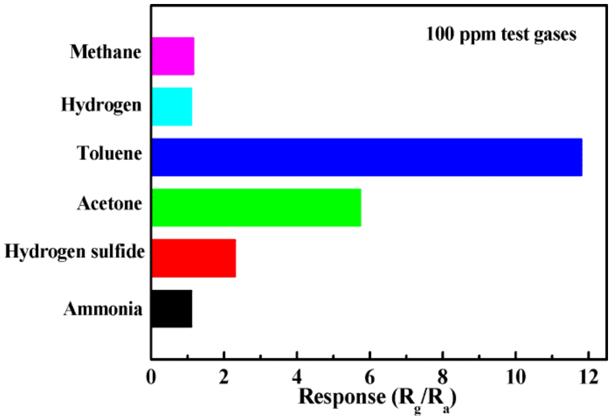

Fig. 6. Selectivity of the porous Co_3O_4 NNWs based sensor to various gases at 150 ℃.

Previous reports about Co_3O_4 based toluene sensors with different morphologies are compared in Table 1. The Co_3O_4 NNWs based sensor in our work has a medium of operating temperature and response. The higher response of ordered mesoporous Co_3O_4 was attributed to high surface area and open mesoporous structure, additionally, a unique one-dimensional nanostructure to nanoparticle-assembled Co_3O_4 nanorods. However, it should be noted that the sensor response can often be influenced by nanostructures of sensing materials and their synthetic methods (requires a bit more thought).

For the gas-sensing mechanism of Co_3O_4 nanomaterials, it should follow a space-charge model.[35, 36] In general, oxygen molecules adsorb on the surface of the sensing materials, and trap electrons from the conduction band of Co_3O_4 to form oxygen species (O_2^-, O_{ads}^{2-}, and O^-), which leads to the increase of charge (hole) concentrations and a widening thickness of charge accumulation layer (the decrease of R_a). When in toluene gas, toluene molecules can react with the adsorbed oxygen species and release the electrons back to Co_3O_4, which results in the decrease of charge (hole) concentrations and the thickness of charge accumulation layer (the increase of R_g).

As we have known, small grain size, high specific surface area and interconnected porous structure of sensing materials can greatly enhance their gas-sensing properties. Fig. 5d shows possible sensing enhancement mechanisms of the sensors based on different microstructures. Co_3O_4 calcined at 350 ℃ maintains the nanosheet architecture and obatins the highest BET surface area (~114.43 $m^2\ g^{-1}$) of three samples, but lacking surface pores (average pore size of 14.31 nm) and a relatively low crystallinity. To a certain extent, it is not conductive to the gas exchange of sensing film and limiting the improvement of sensor performance. As the average pore size increases across the three samples, the Co_3O_4 calcined at 500 ℃ (28.44 nm) has a highly efficient gas exchange for improving sensing performances. However, the compact architectures (~50.78 $m^2\ g^{-1}$) hinder the adsorption of toluene molecules, which leads to low responses in high concentrations of toluene. By contrast, porous Co_3O_4 NNWs prepared at 400 °C have a relatively modest BET surface area (~72.89 m^2 g^{-1}), porous structure (average pore size of 21.48 nm), small grain size and relatively good crystallinity. In particular, the neck-connected intergrain structure of porous Co_3O_4 NNWs makes the sensor resistance can dramatically change in air/toluene gas, which is confirmed to attain an optimized toluene sensing enhancement.

Conclusions

In summary, metastable precursor $Co(OH)_2$ nanosheets, directly prepared by chemical reactions between cobalt nitrate and aqueous ammonia at room temperature, were converted into relatively stable CoOOH nanosheets with the addition of $K_2S_2O_8$. Both of the adding $K_2S_2O_8$ and the amount of aqueous ammonia play key roles in the formation process of CoOOH nanosheets. By controlling the heat treatment at 400 °C for 2 h, a special architecture of porous Co_3O_4 NNWs constructed by neck-connected nanoparticles was obtained. Gas-sensing measurements of the different products prepared in this study indicated that the NNWs based sensor exhibited highest response (R_g/R_a to 100 ppm: 11.79) to toluene at 150 °C, with a low detection concentration of 1 ppm.

Acknowledgements

This work was financially supported by National Natural Science Foundation of China under Grant No. 61176058 and 51202100.

Notes and references

[a] *Key Laboratory of Magnetism and Magnetic Materials of Ministry of Education, Lanzhou University, Lanzhou, 730000, People's Republic of China. Email: xieeq@lzu.edu.cn; zhoujy@lzu.edu.cn. Fax: (+86) 931 8913 554; Tel: (+86) 931 8912 616*

† Electronic Supplementary Information (ESI) available: [TEM images and XRD pattern of CoOOH precursors; EDX spectrum and STEM image of Co_3O_4 NNWs; stability and sensor responses to toluene]. See DOI: 10.1039/c000000x/

1. Y. Liang, Y. Li, H. Wang, J. Zhou, J. Wang, T. Regier and H. Dai, *Nat. Mater.*, 2011, **10**, 780-786.
2. S. Takada, M. Fujii, S. Kohiki, T. Babasaki, H. Deguchi, M. Mitome and M. Oku, *Nano Lett.*, 2001, **1**, 379-382.
3. X. Xia, J. Tu, J. Zhang, X. Huang, X. Wang, W. Zhang and H. Huang, *Electrochem. Commun.*, 2008, **10**, 1815-1818.
4. H.-W. Shim, Y.-H. Jin, S.-D. Seo, S.-H. Lee and D.-W. Kim, *ACS Nano*, 2010, **5**, 443-449.
5. D. Wang, Q. Wang and T. Wang, *Inorg. Chem.*, 2011, **50**, 6482-6492.
6. S. Xiong, C. Yuan, X. Zhang, B. Xi and Y. Qian, *Chem. Eur. J.*, 2009, **15**, 5320-5326.
7. W.-Y. Li, L.-N. Xu and J. Chen, *Adv. Funct. Mater.*, 2005, **15**, 851-857.
8. H. Nguyen and S. A. El-Safty, *J. Phys. Chem. C*, 2011, **115**, 8466-8474.
9. J.-W. Yoon, J.-K. Choi and J.-H. Lee, *Sens. Actuators B: Chem.*, 2012, **161**, 570-577.
10. K.-I. Choi, H.-R. Kim, K.-M. Kim, D. Liu, G. Cao and J.-H. Lee, *Sens. Actuators B: Chem.*, 2010, **146**, 183-189.
11. B. Geng, F. Zhan, C. Fang and N. Yu, *J. Mater. Chem.*, 2008, **18**, 4977-4984.
12. Q. Jiao, M. Fu, C. You, Y. Zhao and H. Li, *Inorg. Chem.*, 2012, **51**, 11513-11520.
13. J. Park, X. Shen and G. Wang, *Sens. Actuators B: Chem.*, 2009, **136**, 494-498.
14. A.-M. Cao, J.-S. Hu, H.-P. Liang, W.-G. Song, L.-J. Wan, X.-L. He, X.-G. Gao and S.-H. Xia, *J. Phys. Chem. B*, 2006, **110**, 15858-15863.
15. M. Tiemann, *Chem. Eur. J.*, 2007, **13**, 8376-8388.
16. J.-H. Lee, *Sens. Actuators B: Chem.*, 2009, **140**, 319-336.
17. T. Wagner, S. Haffer, C. Weinberger, D. Klaus and M. Tiemann, *Chem. Soc. Rev.*, 2013, **42**, 4036-4053.
18. C. C. Li, X. M. Yin, T. H. Wang and H. C. Zeng, *Chem. Mater.*, 2009, **21**, 4984-4992.
19. Y. Fu, X. Li, X. Sun, X. Wang, D. Liu and D. He, *J. Mater. Chem.*, 2012, **22**, 17429-17431.
20. H.-P. Cong and S.-H. Yu, *Cryst. Growth Des.*, 2008, **9**, 210-217.
21. N. Dahal, I. A. Ibarra and S. M. Humphrey, *J. Mater. Chem.*, 2012, **22**, 12675-12681.
22. X. Xia, J. Tu, J. Zhang, X. Huang, X. Wang and X. Zhao, *Electrochim. Acta*, 2010, **55**, 989-994.
23. L. Man, B. Niu, H. Xu, B. Cao and J. Wang, *Mater. Res. Bull.*, 2011, **46**, 1097-1101.
24. J. Xu, L. Gao, J. Cao, W. Wang and Z. Chen, *Electrochim. Acta*, 2010, **56**, 732-736.
25. C. Zhao, J. Fu, Z. Zhang and E. Xie, *RSC Adv.*, 2013, **3**, 4018-4023.
26. L. Birks and H. Friedman, *J. Appl. Phys.*, 2004, **17**, 687-692.
27. H. Cölfen and M. Antonietti, *Angew. Chem. Int. Ed.*, 2005, **44**, 5576-5591.
28. S. Kandalkar, J. Gunjakar, C. Lokhande and O.-S. Joo, *J. Alloys Compd.*, 2009, **478**, 594-598.
29. E. Hosono, S. Fujihara, I. Honma, M. Ichihara and H. Zhou, *J. Power Sources*, 2006, **158**, 779-783.
30. World Health Organization. Air quality guidelines for Europe, 2000.
31. C. Sun, X. Su, F. Xiao, C. Niu and J. Wang, *Sens. Actuators B: Chem.*, 2011, **157**, 681-685.
32. Z. Wen, L. Zhu, W. Mei, Y. Li, L. Hu, L. Sun, W. Wan and Z. Ye, *J. Mater. Chem. A*, 2013, **1**, 7511-7518.
33. S. Liu, Z. Wang, H. Zhao, T. Fei and T. Zhang, *Sens. Actuators B: Chem.*, 2014, **197**, 342-349.
34. L. Wang, J. Deng, Z. Lou and T. Zhang, *Sens. Actuators B: Chem.*, 2014, **201**, 1-6.
35. N. Barsan, C. Simion, T. Heine, S. Pokhrel and U. Weimar, *J. Electrocera.*, 2010, **25**, 11-19.
36. H.-J. Kim and J.-H. Lee, *Sens. Actuators B: Chem.*, 2014, **192**, 607-627.